Weierstraß-Institut
für Angewandte Analysis und Stochastik
Leibniz-Institut im Forschungsverbund Berlin e. V.

Tunable semiconductor ring laser with filtered optical feedback: Traveling wave description and experimental validation

Mindaugas Radziunas[1], Mulham Khoder[2,3], Vasile Tronciu[4], Jan Danckaert[2],

Guy Verschaffelt[2]

submitted: October 17, 2017

[1] Weierstrass Institute
Mohrenstr. 39
10117 Berlin
Germany
E-Mail: mindaugas.radziunas@wias-berlin.de

[2] Applied Physics research group (APHY)
Vrije Universiteit Brussel
Pleinlaan 2
B-1050 Brussels
Belgium
E-Mail: mulham.khoder@vub.ac.be
jan.danckaert@vub.ac.be
Guy.Verschaffelt@vub.be

[3] Brussels Photonics (B-PHOT)
Department of Applied Physics and Photonics
Vrije Universiteit Brussel
Pleinlaan 2
B-1050 Brussels
Belgium

[4] Department of Physics
Technical University of Moldova
bd. Stefan cel Mare 168
Chisinau MD-2005
Republic of Moldova
E-Mail: vasile.tronciu@fiz.utm.md

Tunable semiconductor ring laser with filtered optical feedback: Traveling wave description and experimental validation

Mindaugas Radziunas, Mulham Khoder , Vasile Tronciu, Jan Danckaert, Guy Verschaffelt

Abstract

We study experimentally and theoretically a semiconductor ring laser with four filtering channels providing filtered delayed optical feedback. To describe and analyze the wavelength selection and tuning in this device, we exploit the traveling-wave model determining the evolution of optical fields and carrier density along the ring cavity and filtering branches. The numerical results agree with the experimental observations: we can reproduce the wavelength tuning, the multiple wavelength emission, and the wavelength switching speed measured in these devices. The traveling-wave model allows us to study in detail the effect of the different laser parameters and can be useful for designing the future devices.

1 Introduction

Semiconductor ring lasers (SRLs) are a type of semiconductor lasers which have a circular closed loop cavity shape. Because of this cavity shape, SRLs offer some unique functionalities that are linked to the presence of two directional modes. The directional bistability between the counter propagating fields can be used to obtain all optical switching, optical memories [1, 2, 3] and random numbers generation which is needed for encryption systems [4, 5]. The compact design, the small size, and the possibility to easily integrate a number of SRLs together on the same chip, are the reasons behind recent first attempts to realize an integrated optical neural network based on SRLs [6].

One difficulty when designing/fabricating these SRLs is that there is no strong wavelength selection mechanism in their cavity. Usually, the weak wavelength dependence of the material gain results in the preference of emission in some longitudinal modes (LMs), but the exact emission wavelength is hard to anticipate and control. Moreover, these SRLs can easily become multi-mode for injection currents not close to the lasing threshold and/or changes in the modal composition of the output beam often occur when the SRL's current or temperature are changed.

Many of the possible future applications of SRLs require a specific emission wavelength. For example, if one wants to use them in modern optical telecommunication networks, the emitted wavelength is imposed by the standards of (D)WDM. Besides fixing the emitted wavelength to a specific value imposed by a system or an application, we think these SRLs can become even more interesting if we can actively tune their wavelength. This would open up the perspective of obtaining fully wavelength reconfigurable all optical switches, which require low-cost tunable lasers with sufficient tuning range and output power [7].

There are many different approaches to make a laser wavelength tunable, each approach having its particular advantages and disadvantages. These approaches typically rely on changing the laser's effective cavity length [8], by varying the physical length of the cavity or its refractive index, or by introducing a wavelength dependence in the cavity's gain or loss [9]. Filtered optical feedback (FOF)

is one way of achieving the latter. In this approach, part of the light emitted by the laser is reinjected in the cavity after passing through a wavelength dependent optical filter. The wavelength selective elements in such tunable lasers are thus placed outside of the laser cavity, which can have a positive effect on the stability of the selected wavelength and can result in a simpler control system needed to tune the emitted wavelength [10]. This approach has been implemented successfully in many laser architectures. For example, FOF has been used to make a tunable Fabry-Perot semiconductor laser in [11] and a tunable semiconductor ring laser in [12]. In both of these works, the filtered feedback section has been fabricated on the same chip as the laser, which results in a compact, robust and potentially low-cost device. In [11], the strength of the FOF is controlled by adjusting the current send through semiconductor optical amplifiers (SOAs).

We have combined the electrical control of the FOF from [11] with a SRL, see Fig. 1. We have shown that FOF can be used in SRLs to obtain tunable single mode emission [13] and controllable multi-wavelength emission [14]. We have also shown that the switching from one wavelength to another is rather fast (ns time scale) and is governed by a short transition time together with a not-negligible (longer) delay time at each switching event [15].

In our previous studies about SRLs with FOF, we have used a two-directional mode rate equation model of the SRL [16, 17] extended with Lang-Kobayashi terms to take into account the effect of optical feedback [18, 19]. Different LMs were introduced phenomenologically by including a rate-equation for the (slowly varying) electric field of each mode, whereas the mode coupling was realized through their shared carrier reservoir. This rate equation model does not contain wavelength information of each mode and thus can not reproduce in detail the spectral behavior of the wavelength tunable SRL.

Considering the limitations and the difficulties with the previous model, we use in this paper a traveling-wave (TW) model as a compromise between simplicity and precision [20]. TW models have been used to study the dynamical behavior of different types of semiconductor lasers with a possibility to take into account optical injections, localized reflections and, therefore, delayed feedbacks of the optical fields. Such a TW model for SRLs considers the CW and CCW propagating slowly varying optical fields governed by the TW equations which are mutually coupled through linear backscattering terms, through nonlinear cross- and self- saturations, and through the spatially parameterized carrier rate equation [20, 21]. This approach allows simulating ring structures taking into account the longitudinal distributions of the carriers and of the optical fields in a natural way. The TW model has been used to explain the dynamical characteristics of SRLs such as lasing direction hysteresis [20], directional switching [22] and Four Wave Mixing (FWM) in SRLs subject to optical injection [23].

In this work, we demonstrate that the TW model can successfully reproduce the impact of the FOF on the behavior of the SRL. We concentrate on the spectral changes in the laser output under the effect of FOF: we show how the emitted wavelengths change when different control currents are tuned. The results achieved using the TW model are in good agreement with experimental results. Using this model, we can study in detail the effect of the different laser parameters, which is often impossible in experiments as changing an injected current usually influences several parameters at once: for example, the current injected into an active region changes both the gain and the refractive index. In our opinion, simulations and analysis of the TW model can be extremely helpful when designing new SRL devices.

Our paper is organized as follows. In Section 2 we introduce the device layout and present the experimental results. In Section 3 we present the model equations describing different parts of the SRL and the field transmission/reflection/outcoupling conditions at different interfaces of the complex SRL device. Section 4 is devoted to simulations and analysis of the SRL dynamics under different driving conditions. At the end of the paper some conclusions are drawn.

2 Experimental setup and measurements

In this section, we briefly introduce our experimental SRL device and present its typical operation under different driving conditions.

Description of the device. Our experimental device consists of the SRL and four FOF branches fabricated on the same chip by the JePPIX platform [24]. The mask layout and the schematic representation of the device are shown in Fig. 1. The ring cavity of the SRL has a race-track geometry with two straight active waveguides, each $753\,\mu$m long, connected to each other via two passive, curved waveguides with a bend radius of $107\,\mu$m. The circumference of the ring defines the mode spacing. The filtered feedback part of the device includes two identical arrayed-waveguide grating (AWG) filters, each connected to the SRL by a single waveguide and both mutually connected to each other through four outputs. The AWGs are used to split the optical fields emitted by the SRL into four different wavelength channels, each supporting a few LMs of the SRL: whereas the AWG channel spacing is $1.41\,$nm and the AWG free spectral range is $5.65\,$nm, the LM spacing is $0.3\,$nm. Four electrically controllable SOA gates are located in the middle of the four waveguides connecting the two AWGs with each other. Each of these SOAs can be independently pumped with an electrical bias current using a metallic contact pad, what allows for an efficient control of the feedback strength in each FOF branch.
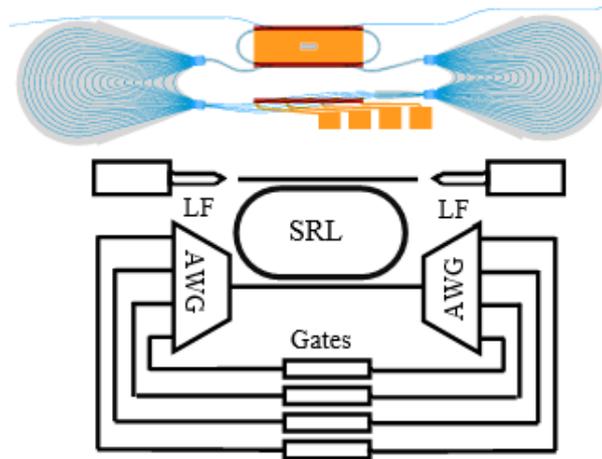

Figure 1: The mask layout (top) and the schematic representation (bottom) of the considered SRL with four branches of the FOF. AWG: Arrayed Waveguide Grating, LF: Lensed Fiber.

The device chip is mounted on a brass submount. A $10\,$kΩ thermistor and a Peltier element are placed beneath the submount to stabilize the laser temperature at $21°$C. Two lensed fibers (one in the CW and another one in the CCW direction) are used to collect the device output. We use electrical probes to bias the SRL and the SOA gates. The device's output waveguide has an angle of $7°$ with respect to the chip facet in order to reduce the reflections from the edge of the chip. To introduce some asymmetry in the field reflectivities on the right-hand side facet of the device in Fig. 1, we have applied an additional anti-reflection coating. More details on the fabrication and the layout of the device can be found in [13].

SRL with suppressed FOF. In our first set of measurements we have analyzed the performance of the SRL device with all FOF branches being unbiased ($I_1 = \ldots = I_4 = 0$), see Fig. 2. The optical feedback, in this case, is strongly suppressed, and the measured performance of our device is typical

for solitary SRLs. The power-current characteristics in Fig. 2(a) reveal the bidirectional operation of the laser immediately after the lasing threshold at $I_R \approx 65$ mA. This bidirectionality is mainly induced by the presence of the field backscattering due to the deep etching of the waveguides and the nonvanishing reflectivities at the directional couplers and facets. On the other hand, the (small) asymmetry of the facet reflectivities guarantees the dominance of the CW field. An increase of the bias current I_R results in sporadic switchings between LMs (see panel (b) of the same figure) related to the jumps of the emission intensities shown in panel (a). It is noteworthy, that whereas for the smaller currents the laser behavior is mostly determined by a single LM with a side mode suppression ratio (SMSR) of more than 20dB (see panel (c)), for the larger currents a strongly pronounced multi-mode behavior is observed (see panel (d) of the same figure).
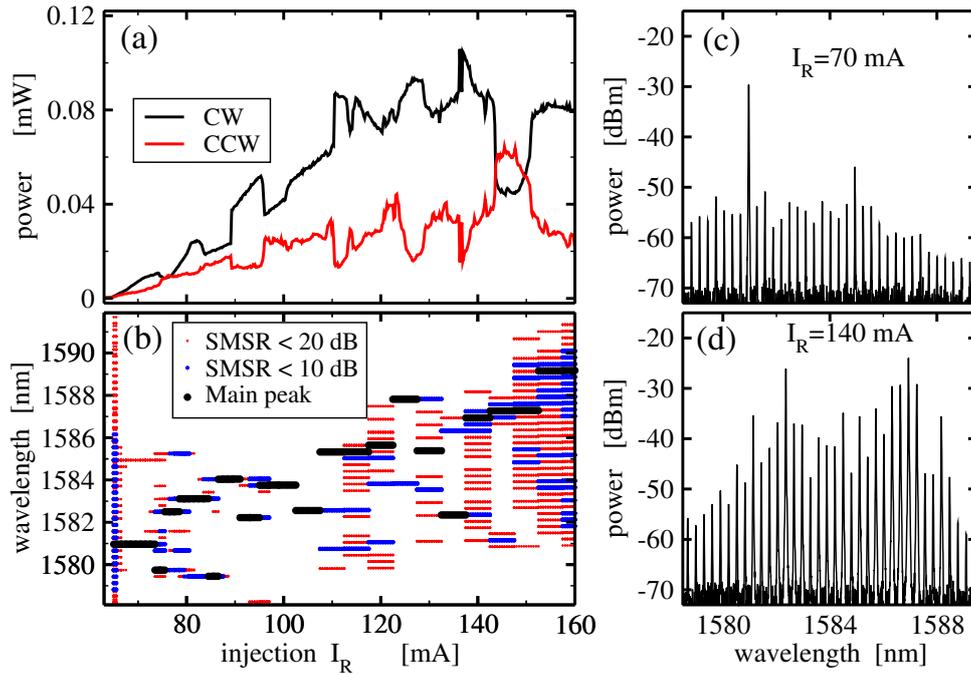

Figure 2: Measurements of the SRL device with uninjected FOF. Intensities of the emitted CW (black) and CCW (red) fields (a) and main lasing wavelengths of the CCW field (b) as functions of the total ring laser current I_R. Large, medium, and small bullets in panel (b) represent the main spectral peak and all side peaks suppressed by less than 10 dB and less then 20 dB, respectively. (c) and (d): optical spectrum of the CW field at $I_R = 70$ mA and 140 mA, respectively.

SRL with enhanced FOF. In the next step, we investigate the effect of the FOF on the device's output. Pumping of one or a few gates results in the transmission (or even amplification) of the corresponding LMs through the corresponding branches of the FOF, what in its turn leads to the dominance of these modes in the SRL. An example of such operation for an SRL bias of $I_R = 85$ mA is presented in panels (a) and (b) of Fig. 3. In the case of unbiased gates, the SRL shows a multimode emission. Once we apply 45 mA bias current to one of the gates (schematically indicated on the top part of these diagrams), the SRL device shows a single LM emission with > 20 dB SMSR within the transmission band of the biased gate, see Fig. 3 (a). By a careful choice of the bias currents at a pair of the gates, we can also realize a corresponding dual mode operation, see, e.g., Fig. 3 (b).

The level of the SRL and gate pumpinghas a large impact on the emission characteristics. For example, Fig. 3 (c) represents a typical power-current characteristic diagram of the SRL device with the
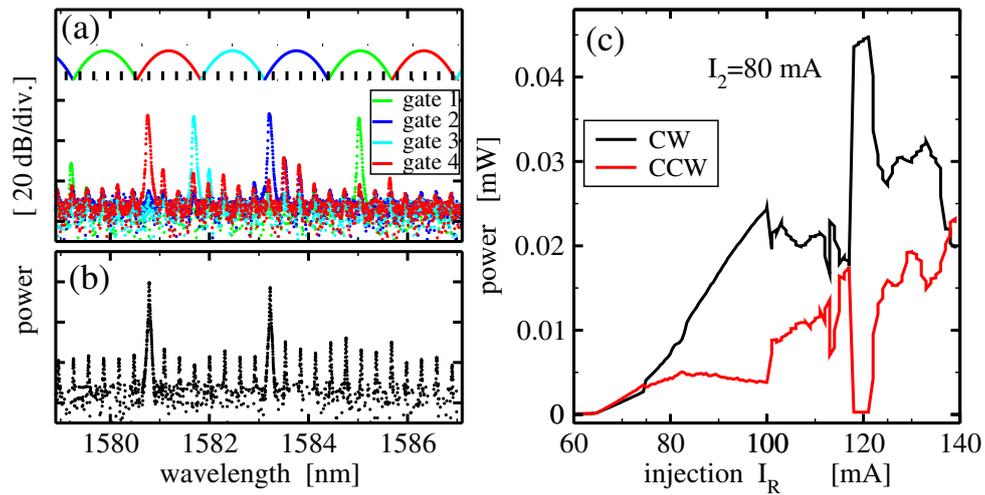
Figure 3: Left: selected optical spectra in CW direction of the SRL device with $I_R = 85mA$ and the single gate current of 45 mA (a), or for the dual gate pumping with $I_2 = 19.92$ mA and $I_4 = 11.84$ mA (b). Green, blue, cyan and red colors in panel (a) indicate the biased gate. The LMs of the SRL and the AWG channel passbands are plotted as a reference on the top this panel. (c): output power from CW (black) and CCW (red) directions as functions of the current injected into the SRL whereas the second gate bias $I_2 = 80$ mA.

activated second gate, $I_2 = 80$ mA. It is evident that whereas the lasing threshold remains more or less the same as in the case of an unbiased gate, see Fig. 2(a), the selection of the LMs and the contributions of the CW and CCW fields to the total emission now are fully determined by the interaction of a limited amount of LMs supported by the second FOF channel (henceforth called second channel LMs).

Concluding this section, we should note, that the SRL device described above and some of the measurements have been already discussed in Refs. [13, 14]. The main reason for presenting these experiments again is their comparison with our new calculations of this device using the TW model. This model and our new theoretical findings are discussed in the following sections.

3   Theoretical Model

In order to model the ring laser with several feedback branches, we use the Traveling Wave model [25] describing the evolution of the complex amplitudes of the slowly varying counter-propagating optical fields and spatially distributed carrier density within the active parts of the device. This dynamic PDE model has a single spatial dimension corresponding to the direction along the ring cavity, outcoupling waveguide, and all feedback branches. Our modeling approach allows simulating various multisection lasers, ring structures and coupled laser systems. It can take into account optical injections, localized reflections and, therefore, delayed feedback of the optical fields [26, 27]. Schematically all these lasers can be represented as graphs consisting of different *sections* (edges of the graph) mutually interconnected at multiple *junctions* (vertices of the same graph).

Laser setup.   The scheme of the SRL with four separate FOF branches simulated and analyzed in this paper is given in Fig. 4. *Sections* and *junctions* of the device are indicated by colored frames
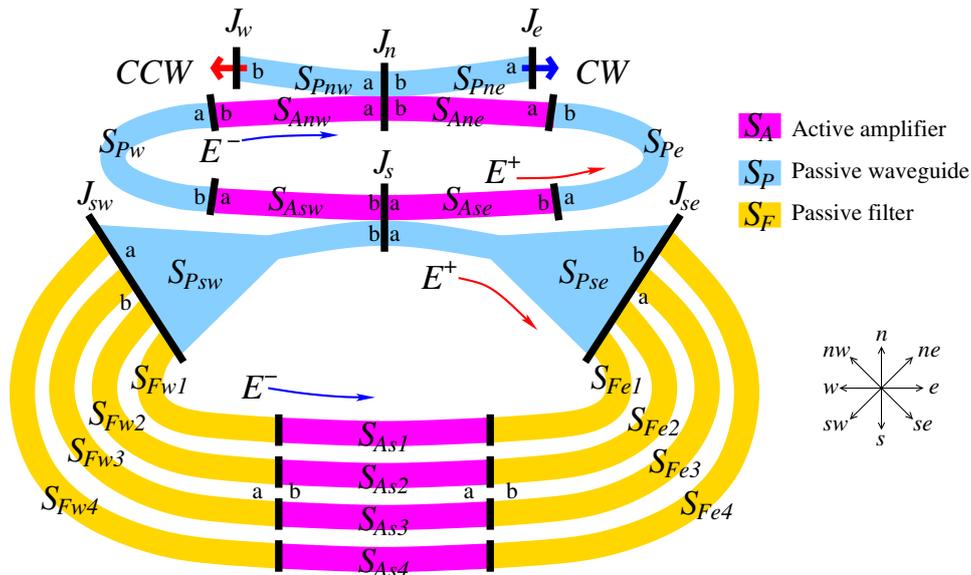
Figure 4: Schematic representation of the simulated integrated SRL with four branches of filtered and amplified bidirectional optical feedback. Black segments and colored frames indicate different junctions and sections of the SRL. Red and blue arrows show propagation directions and the emission of the CCW and CW fields E^+ and E^-, respectively.

and thick black segments, respectively. Here, the frames of different colors indicate different types of the device sections. More particularly, we distinguish the amplifying sections and two types of the passive sections. In the active sections, $S_{A.}$, the field equations are nonlinearly coupled to the spatially parameterized carrier rate equation. In the passive sections, carrier dynamics is irrelevant, whereas propagating complex optical fields undergo attenuation, phase shift (passive waveguide sections $S_{P.}$), and an eventual frequency filtering (optical filter sections $S_{F.}$).

When required to distinguish model parameters within different sections and the sections themselves, we use different subscript indices. Moreover, for each section S_j we attribute a unique spatial segment $[a_j, b_j]$, where b_j and a_j are "front" and "rear" edges of this section (see Fig. 4), $b_j > a_j$, and $|S_j| = b_j - a_j$ is the section length. The notations of all sections in Fig. 4 are made according to the cardinal directions *n*, *e*, *s*, and *w*.

Note, that in contrast to the experimental setup [Fig. 1(b)], the field transition from the ring to the out-coupling waveguide or the feedback loops and vice versa is localized at the single point corresponding to the center of the "northern" (junction J_n in Fig. 4) and "southern" (junction J_s in the same figure) part of the main ring amplifier. As a consequence, these artificially introduced junctions in our model split the corresponding parts of the real device into pairs of adjacent "sections" (S_{Pnw} and S_{Pne}, S_{Anw} and S_{Ane}, e.t.c.).

Model equations in the laser sections.   The evolution of the CCW optical field $E^+(z,t)$ and the CW field $E^-(z,t)$ within each (active or passive) section S_j of the device are governed by the TW equations

$$i\frac{n_g}{c_0}\partial_t E^\pm = \left(\mp i\partial_z + \beta^\pm - i\mathcal{D}\right)E^\pm + F^\pm_{sp}, \qquad (1)$$

where $|E|^2 = |E^+|^2 + |E^-|^2$ is the local photon density (proportional to the local field intensity). c_0 is the speed of light in vacuum, n_g is the group velocity index, and $F^\pm_{sp}$ is the Langevin noise source

contribution to the optical fields.

The linear operator $\mathcal{D}$ is used to describe optical frequency filtering effects on the propagating optical fields defined in the time domain. We assume a Lorentzian profile of such a filtering in the optical frequency domain,

$$\mathcal{D}\widehat{E}^{\pm}(z,\omega) = \frac{\bar{g}}{2}\frac{i(\omega-\bar{\omega})}{(\bar{\gamma}/2)+i(\omega-\bar{\omega})}\widehat{E}^{\pm}(z,\omega).$$

Here, $\bar{g}$, $\bar{\gamma} = \frac{2\pi c_0}{\lambda_0}\bar{\gamma}_\lambda$, and $\bar{\omega} = -\frac{2\pi c_0}{\lambda_0}\bar{\lambda}$ are the amplitude, the full width at the half maximum, and the peak frequency (relative to the central frequency $\omega_0 = \frac{2\pi c_0}{\lambda_0}$) of this Lorentzian, respectively. λ_0 is the central wavelength, whereas $\bar{\gamma}_\lambda$ and $\bar{\lambda}$ are wavelength domain representations of the filter width and peak position, respectively. The Lorentzian profile assumption allows an easy replacement of the nonlocal operator $\mathcal{D}$ by the first order ODE for the newly introduced complex functions $P^+(z,t)$ and $P^-(z,t)$ [25, 28]:

$$\mathcal{D}E^{\pm} = \frac{\bar{g}}{2}\left(E^{\pm} - P^{\pm}\right), \quad \partial_t P^{\pm} = \frac{\bar{\gamma}}{2}\left(E^{\pm} - P^{\pm}\right) + i\bar{\omega}P^{\pm}. \tag{2}$$

We apply this approach to model optical filtering in passive sections $S_{F.}$ and material gain dispersion in all active sections $S_{A.}$, whereas in the passive waveguiding sections $S_{P.}$ we set $\mathcal{D} = 0$.

The propagation factors β^+ for the field E^+ and β^- for the field E^- in Eq. (1) are defined by

$$\beta^{\pm} = \left[\delta_0 - \frac{i\alpha}{2}\right] + \frac{\alpha_H g(N)}{2} + \frac{ig(N)}{2(1+\varepsilon_s|E^{\pm}|^2+\varepsilon_c|E^{\mp}|^2)}, \tag{3}$$

where real parameters δ_0, α, α_H, ε_s, and ε_c are the frequency detuning, the internal absorption of the fields, the linewidth enhancement factor, the self- and cross- gain saturation factors, respectively. We note here, that introduction of different factors ε_s and ε_c is less important for linear laser devices but is crucial when modeling ring lasers [17, 21].

Whereas in the passive sections the material gain function $g(N)$ is set to zero, in the active sections it is given by the following logarithmic dependence on the carrier density $N(z,t)$:

$$g(N) = g'N_{tr}\ln\left(\frac{\max\{N,N_*\}}{N_{tr}}\right). \tag{4}$$

Here, the parameters N_{tr} and g' are the carrier density at the transparency, $g(N_{tr}) = 0$, and the effective differential gain including lateral confinement factor, $g' = \frac{dg(N_{tr})}{dN}$, respectively. The introduction of the small carrier density N_* in Eq. (4) allows avoiding too large field absorption when $N \ll N_{tr}$.

The carrier density $N(z,t)$ within each active section S_{Aj} is governed by the carrier rate equation

$$\partial_t N = \left[\frac{I}{q\sigma|S|} + \frac{U_F'[\langle N\rangle-N]}{R_s q\sigma|S|}\right] - \left(AN + BN^2 + CN^3\right)$$
$$- \frac{c_0}{n_g}\Re\sum_{\nu=\pm}E^{\nu*}\left[\frac{g(N)}{1+\varepsilon_s|E^\nu|^2+\varepsilon_c|E^{-\nu}|^2} - 2\mathcal{D}\right]E^\nu, \tag{5}$$

where the first, the second, and the third terms at the right-hand side of this equation model the inhomogeneous current injection [29, 28], the spontaneous- and stimulated recombination, respectively. $\langle N\rangle(t) = \frac{1}{|S|}\int_S N(z,t)dz$ is the sectional average of the carrier density, q is the electron charge, whereas I, σ, U_F', R_s, A, B, and C are the injected current into the considered section S, the cross-section area of the active zone, the derivative of the Fermi level separation with respect to N, the series resistivity, and three spontaneous recombination parameters, respectively.

Finally, to model thermal shifts of the operating wavelengths occurring once changing bias currents, we assume simple linear dependencies of the frequency detuning term δ_0 and the gain peak wavelength $\bar{\lambda}$ on the bias current I [30, 31] :

$$\delta_0 = \frac{2\pi n_g}{\lambda_0^2}\left(\delta_{\lambda,st} + c_T I\right), \qquad \bar{\lambda} = \bar{\lambda}_{st} + d_T I, \tag{6}$$

where $\delta_{\lambda,st}$ and $\bar{\lambda}_{st}$ are static injection-independent contributions to these parameters in the wavelength domain, whereas constants c_T and d_T represent changes of these parameters when tuning the bias current I.

Field scattering at the junctions. To close the TW model equations (1), we need to set the values of the fields E^+ at "rear" edges a_j, and the values of E^- at "front" edges b_j of all sections S_j. Thus, we need to define the field scattering (transmission-reflection) conditions at each junction J_s indicated by thick black segments in Fig. 4. In this work, we assume trivial scattering conditions (lossless transmission, vanishing reflectivity) at each simple interface of two adjacent sections S_j and S_k (assuming that the section edges coincide, i.e. $b_j = a_k$):

$$E^+(a_k, t) = E^+(b_j, t), \quad E^-(b_j, t) = E^-(a_k, t). \tag{7}$$

At the outer edges of the outcoupling waveguide (junctions $J_w \equiv b_{Pnw}$ and $J_e \equiv a_{Pne}$ in Fig. 4), we suggest simple reflection-transmission conditions. Here,

$$\begin{aligned}
E^-(b_{Pnw}, t) &= r_w E^+(b_{Pnw}, t), \quad E_{out}^+(t) = t_w E^+(b_{Pnw}, t), \\
E^+(a_{Pne}, t) &= -r_e^* E^-(a_{Pne}, t), \quad E_{out}^-(t) = t_e E^-(a_{Pne}, t), \\
|r_s| &\le 1, \qquad t_s = \sqrt{1 - |r_s|^2}, \qquad s = e, w.
\end{aligned} \tag{8}$$

$E_{out}^+(t)$ and $E_{out}^-(t)$ denote the emitted CCW and CW fields at these edges, whereas t_s and r_s are real transmission and complex reflection factors of the optical field amplitude at the junction J_s, $s = e, w$.

At the junctions $J_{sw} \equiv b_{Fwj} = a_{Psw}$ and $J_{se} \equiv a_{Fej} = b_{Pse}$, $j = 1, \ldots, 4$, (see again Fig. 4) we neglect all possible reflections and use the following scattering conditions

$$\begin{aligned}
E^+(a_{Psw}, t) &= \textstyle\sum_{j=1}^4 E^+(b_{Fwj}, t), \\
E^-(b_{Fwj}, t) &= \tfrac{1}{2} E^-(a_{Psw}, t), \qquad j = 1, \ldots, 4, \\
E^-(b_{Pse}, t) &= \textstyle\sum_{j=1}^4 E^-(a_{Fej}, t), \\
E^+(a_{Fej}, t) &= \tfrac{1}{2} E^+(b_{Pse}, t), \qquad j = 1, \ldots, 4,
\end{aligned} \tag{9}$$

which, after ignoring rapidly oscillating products of the fields in different filtering channels, $\Re E^+(b_{Fwj}, t) E^{+*}(b_{Fwk}, t)$ and $\Re E^-(a_{Fej}, t) E^{-*}(a_{Fek}, t)$, $k \ne j$, guarantee the conservation of the field intensity before and after the scattering.

Finally, at the ring outcoupling junctions $J_n \equiv a_{Anw} = b_{Ane} = a_{Pnw} = b_{Pne}$ and $J_s \equiv a_{Ase} = b_{Asw} = a_{Pse} = b_{Psw}$, we take into account field transmissions to both sections located at the opposite side of the junction and we assume small backscattering reflections:

$$\begin{aligned}
E^+(a_{Alj}, t) &= t_l E^+(b_{Al\bar{j}}, t) + i\tilde{t}_l E^+(b_{Pl\bar{j}}, t) - r_l^* E^-(a_{Alj}, t), \\
E^+(a_{Plj}, t) &= t_l E^+(b_{Pl\bar{j}}, t) + i\tilde{t}_l E^+(b_{Al\bar{j}}, t) + r_l^* E^-(a_{Plj}, t), \\
E^-(b_{Al\bar{j}}, t) &= t_l E^-(a_{Alj}, t) + i\tilde{t}_l E^-(a_{Plj}, t) + r_l E^+(b_{Al\bar{j}}, t), \\
E^-(b_{Pl\bar{j}}, t) &= t_l E^-(a_{Plj}, t) + i\tilde{t}_l E^-(a_{Alj}, t) - r_l E^+(b_{Pl\bar{j}}, t), \\
t_l &= i\sqrt{1 - \tilde{t}_l^2 - |r_l|^2}, \qquad (l, j, \bar{j}) \in \{(n, w, e), (s, e, w)\}.
\end{aligned} \tag{10}$$

Here again, the assumption that the outcoupling transmission factor $\tilde{t}_l$ is real implies the conservation of the field intensity before and after the scattering.

We should note, however, that the scattering relations defined above allow to close the TW model (1)-(4) but neglect some properties of real devices. A more detailed estimation of the transmission -

reflection - outcoupling relations requires an advanced modeling, which takes into account the curvature of the ring cavity, the length of the coupling regions, the frequency of the fields, the field diffraction, and the overlapping of the lateral modes in the coupling region [32], but such modeling is outside the scope of this paper.

Parameters. In our modeling approach, the considered SRL with four branches of FOF has 22 "sections" and 18 "junctions", see Fig. 4, and each of these objects, in general, has his own set of parameters. Fortunately, some of the parameters attributed to all or some groups of sections are the same. For example, in all sections we use the same group index $n_g = 3.65$.

For the passive waveguiding sections, S_P. (light blue), we use $|S_{Pe}| = |S_{Pw}| = 340\,\mu$m, $|S_{Pne}| = |S_{Pnw}| = 2000\,\mu$m, $|S_{Pse}| = |S_{Psw}| = 2500\,\mu$m as this corresponds to the physical length of the device. The gain function $g(N)$, the Lorenzian gain amplitude $\bar{g}$, and the frequency detuning δ_0, in these sections are set to zero, whereas the absorption factor $\alpha = 1\,$cm^{-1}.

For the passive filtering sections, S_F. (yellow), we use $|S_F.| = 530\,\mu$m. We assume vanishing $g(N)$ and δ_0, and the field absorption $\alpha = 5\,$cm^{-1}. The Lorentzian gain amplitude and full width at half maximum are set to $\bar{g} = 500\,$cm^{-1} and $\bar{\gamma}_\lambda = 4\,$nm. The relative peak wavelengths of four filtering branches (sections S_{Fwj} and S_{Fej}, $j = 1, \ldots, 4$) are set to $\bar{\lambda} = -2.15\,$nm, $-0.705\,$nm, $0.705\,$nm, and $2.15\,$nm, respectively, such that the channel spacing is $1.41\,\mu$m as in the experimental device.

For the amplifying sections (pink) within the SRL (S_{Ajk}, $j = n, s$, $k = e, w$) and within the four filtering branches (S_{Asr}, $r = 1, \ldots, 4$) we set $|S_{Ajk}| = 380\,\mu$m and $|S_{Asr}| = 190\,\mu$m, respectively. The remaining parameters in all these sections are $\alpha = 1\,$cm^{-1}, $g' = 6 \cdot 10^{-21}\,$m^2, $N_{tr} = 10^{24}\,$m^{-3}, $N_* = 0.02 \cdot 10^{24}\,$m^{-3}, $\alpha_H = -4$, $\varepsilon_s = 10^{-25}\,$m^3, $\varepsilon_c = 2\varepsilon_s = 2 \cdot 10^{-25}\,$m^3, $\bar{g} = 100\,$cm^{-1}, $\bar{\gamma}_\lambda = 100\,$nm, $\sigma = 0.24\,\mu$m^2, $R_s = 5\,\Omega$, $U'_F = 10^{-25}\,$Vm^3, $A = 0.9 \cdot 10^9\,$s^{-1}, $B = 10^{-16}\,$m^{3}s^{-1}, $C = 2 \cdot 10^{-41}\,$m^{6}s^{-1}. In all our calculations the currents within the four active ring sections, S_{Ajk}, $j = n, s$, $k = e, w$, are kept the same, $I = I_R/4$. The total ring laser current I_R as well as currents I_j in amplifying sections of the FOF branches, S_{Asj}, $j = 1, \ldots, 4$, are used as control parameters of the considered system. In the case of the switched-off FOF branches (currents I_j of the sections S_{Asj} are set to zero), the threshold current $I_{R,thr} \approx 65\,$mA. To define the frequency and the gain peak detuning, we set $\delta_0 = \bar{\lambda} = 0$ in the amplifiers S_{Asr} of the FOF branches, and $\delta_{\lambda,st} = -0.5\,$nm, $\bar{\lambda}_{st} = -5\,$nm, $c_T = 18.5\,$nm/A, and $d_T = 160\,$nm/A, in the active sections of the main SRL.

The field transmission and reflection conditions (10) at J_n and J_s are entirely determined by the outcoupling transmissions $\tilde{t}_n = \tilde{t}_s = \sqrt{0.3}$ and small backscattering reflections $r_n = r_s = 0.005$. The asymmetric reflection conditions (8) at the outer edges of the outcoupling waveguide, J_e, J_w, are defined by $r_e = 0.01$ and $r_w = -0.1$, respectively. The central wavelength is $\lambda_0 = 1.58\,\mu$m.

Some of these parameters (e.g., lengths of the sections, widths and depths of the active zone, widths and central wavelengths of the filtering elements) are taken directly from the design layout. Some other parameters (e.g., a group velocity factor, a central wavelength, thermal tuning factors) were estimated from experimental data. A majority of the remaining parameters (differential gain, threshold carrier density, scattering losses, carrier recombination and gain dispersion parameters) are typical for similar lasers and were slightly adapted to fit the lasing threshold. To define reasonable field absorption in the FOF branches, gain saturation parameters, and asymmetric field reflection-transmission conditions, we have performed an extensive numerical study seeking to obtain a similar behavior as in the experiments.

4   Theoretical results

Simulations of the SRL with suppressed FOF.   First of all, we have performed a set of simulations of our SRL with uninjected FOF gates, see Fig. 5. Similarly to experiments (Fig. 2), the simulated SRL provides bidirectional and mostly multi-mode emission with the CW field being slightly dominant, which is mainly due to the asymmetry of the field reflections at the facets of the device. Small variations of the field reflectivity phases $\arg(r_j)$ at the *junctions* or of the detuning factors δ_0 at the different sections of the device introduce changes of the phase relations between optical fields, and, consequently, can be used for adjusting bifurcation (mode jump) positions as well as longitudinal mode distributions or CW and CCW emission intensities in the parameter-tuning calculations [21, 27]. Since the exact values of all these parameters are not known, it is hard to find a perfect fit of the simulated and measured results.

It is noteworthy that in our simulations these gates are not fully deactivated, i.e. the field is not fully absorbed in the SOAs. Part of the optical fields at certain wavelengths can go through the gates and be reinjected into the main SRL. This fact is illustrated by instantaneous (gate carrier-dependent) transmission spectra of the four FOF branches at the top of the panels (c)-(e). Thus, formally being closed, these gates still provide some weak LM selection mechanism.
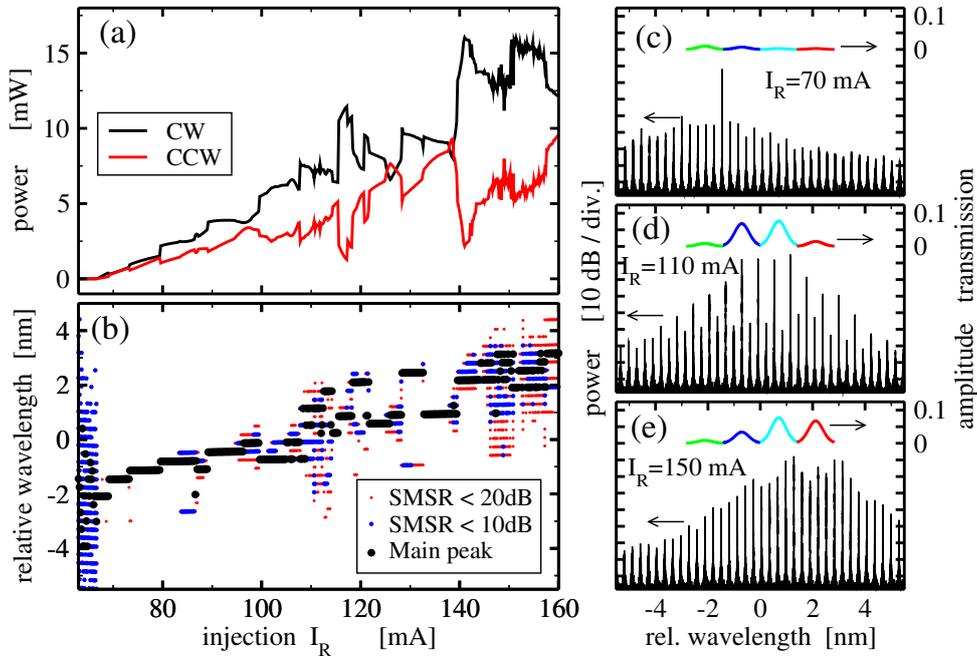

Figure 5: Simulated performance of the SRL with uninjected FOF. (a) and (b): the same as in experimental figures 2(a) and (b). (c)–(e): optical spectra of the CW emission at $I_R = 70$ mA, 110 mA, and 150 mA. Corresponding instantaneous field amplitude transmission spectra for all four FOF branches are plotted on the top of these panels.

In experiments, we do not have any direct access to the FOF branch transmission spectra. The nonvanishing field transmittance through one or another branch, however, can be suspected when analyzing measured optical spectra, see Fig. 2(b)-(d). Large optical injection into an unpumped gate reduces the field absorption. This permits weak transmission of several LMs located within periodically reappearing AWG channel passbands. This slight enhancement of a single channel transmission nicely explains the presence of ~ 5.65 nm separated large intensity LM clusters in measured optical spectra, see Figs. 2(d) and (b).

In contrast to the experimental device, the periodic reappearance of the AWG channel passband is not included in our model: each opened or weakly opened gate supports only a few neighboring LMs. For this reason, the width of the simulated optical spectra is limited by $\sim 5.65\,\mathrm{nm}$ (which is a combined width of four modeled channeled bands) and, usually, is smaller than the width of the measured spectra, compare Figs. 2(b) and 5(b).

Thermal detuning. The thermal shift of the material gain peak position $\bar{\lambda}$ modeled by the nonvanishing factor $d_T \approx \frac{\Delta\bar{\lambda}}{\Delta I_R/4}$ in Eq. (6) (here and below Δf denotes a change of the factor f) induces the general redshift of the optical spectra, see Fig. 5(b). The value of this parameter was set assuming $4\,\mathrm{nm}$ linear redshift of the gain peak position $\bar{\lambda}$ once the ring cavity current I_R was changed from 60 to $160\,\mathrm{mA}$.

The nonvanishing factor c_T in Eq. (6) implies a small-scale redshift $\frac{\Delta\lambda}{\Delta I_R}$ of the LM wavelengths λ with the change of the bias current I_R. In the experiments, this shift was $\approx 3.2\,\mathrm{nm/A}$. It is known [21] that variations of the cumulative factor $\Re\beta$ in the ring cavity imply corresponding changes in the optical frequencies (and wavelengths) of the LMs:

$$\begin{aligned}
\Delta\Re\Omega &= -\frac{2\pi c_0}{\lambda_0^2}\Delta\lambda \approx -\frac{1}{\tau}\int_{S_R}\Re\Delta\beta(z)dz \\
&= -\frac{1}{\tau}\frac{2\pi n_g}{\lambda_0^2}|S_{RA}|c_T\Delta I_R/4 - \frac{1}{\tau}\frac{\alpha_H}{2}\int_{S_{RA}}\Delta g(N(z))dz,
\end{aligned}$$

where S_R and S_{RA} denote the whole SRL and its all active sections, whereas $\tau = \frac{|S_R|n_g}{c_0}$ is the field roundtrip time in the SRL. For the SRL operating above threshold, the expected mean change of the gain $g(N(z))$ is weak, such that the last term in the formula above can be omitted. As a consequence, a small-scale tuning of the LM wavelengths is mainly induced by the injected current, what immediately allows to estimate the tuning factor: $c_T \approx \frac{\Delta\lambda}{\Delta I_R/4}\frac{|S_R|}{|S_{RA}|}$, where the factor c_T in all four active sections of the ring is the same.

Both above discussed thermal shifts are the main reason of the experimentally and theoretically observed jumps between different LMs.

SRL with a single activated branch of the FOF. In the next step, we perform a similar study of the SRL with a single activated branch of the FOF. We adjust the second branch gate current $I_2 = 80\,\mathrm{mA}$ and tune the ring bias current I_R. This numerical experiment mimics the set of measurements presented in Fig. 3(c).

After inspection of the power-current and the wavelength-current characteristics in panels (a) and (b) of this figure one can get an impression that the dynamics of this laser is rather simple and is mainly determined by a single LM selected by the second FOF branch. A more detailed study of the laser operation reveals the existence of multiple non-stationary regimes indicated by the gray shading in panels (a) and (b). Whereas at smaller currents I_R these regimes are mainly simple transients associated with the exchange of the field intensity between adjacent LMs, for larger I_R these states can be much more interesting from the dynamic point of view. An example of such regime calculated at the fixed $I_R = 120\,\mathrm{mA}$ is represented in panels (c) and (d) of the same figure. In this case, we have a stable dual-oscillatory regime defined by two different periods, $\tau_{AO} \approx 2.75\,\mathrm{ns}$ and $\tau_0 \approx 209\,\mathrm{ps}$, see panel (c), or, equivalently, by different separations of the corresponding spectral lines, $\Delta_{AO} \approx 3\,\mathrm{pm}$ and $\Delta_0 \approx 40\,\mathrm{pm}$, see both inserts of the panel (d).

The factor τ_0 in our case is close to the doubled sum of the field propagation time in the SRL ($\tau_R \approx 26.77\,\mathrm{ps}$, $\Delta_R \approx 311\,\mathrm{pm}$) and the FOF branch ($\tau_F \approx 76\,\mathrm{ps}$, $\Delta_F \approx 109.5\,\mathrm{pm}$). Our simulations

have shown that this characteristic time depends on the lasing mode wavelength (e.g., $\tau_0 \approx 179\,\text{ps}$ once lasing is determined by the first FOF branch) but otherwise remains nearly independent on the changes of different control parameters.
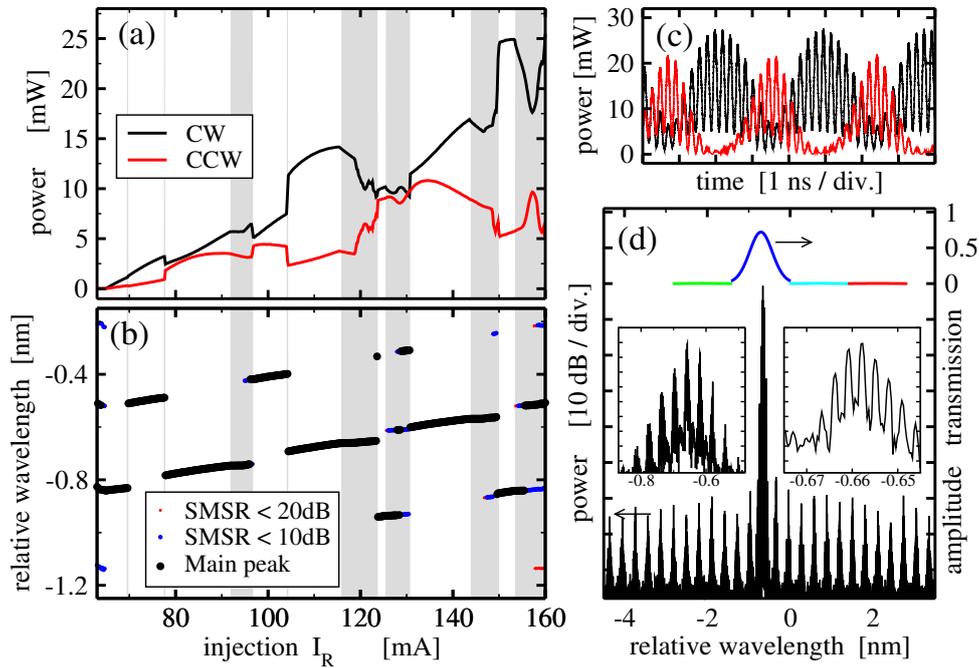

Figure 6: Simulated performance of the SRL with an injected second FOF gate ($I_2 = 80\,\text{mA}$). (a) and (b): the same as in corresponding panels of Figs. 2 and 5. Gray shading shows the regions where nonstationary regimes are observed. (c) and (d): the time-traces of the emitted CW/CCW (black/red) fields and the optical spectra of the CW field representing dynamics of the laser at $I_R = 120\,\text{mA}$. Transmission spectra for all four FOF branches are plotted on the top of panel (d). Inserts in the same panel are the enlarged images of the main spectral peak.

The slow oscillations at τ_{AO} are characterized by the alternating intensities of the counterpropagating fields. The oscillations are rather typical for the SRLs [16, 17]. The period τ_{AO} is not related to τ_R nor to τ_F. According to Ref. [21], it depends on the field reflectivity/transmission parameters at the inner interfaces of the SRL (which are fixed in our simulations) and the cumulative difference $\Delta_\beta = \langle \beta^+ - \beta^- \rangle$ of the propagation factors in the SRL. Due to nonvanishing self- and cross-gain saturation, the factors β^+ and β^- depend on the CW and CCW field distributions. Thus, in different simulations, the cumulative difference Δ_β and, consequently, the alternate oscillation (AO) period τ_{AO} are changing.

Impact of the field feedback phase to the LM selection. The phase of the complex optical fields in the FOF branches is determined by the actual field frequency (or wavelength) and the real parts of the propagation factors $\beta^\pm$. In general, the variation of gate currents implies thermal ($\sim c_T I$) and electronic ($\sim \alpha_H g(N)$) changes of this phase. For a better understanding of the phase tuning effect, in what follows we will fix all bias currents and redefine the detuning factor δ_0 for each j-th FOF gate in Eq. (6) as $\delta_0 = \delta_{0,st} + \frac{\varphi_j}{|S_{SAj}|}$. The tuning of φ_j in the j-th gate implies a shift of the phase relation of the same directional fields at the beginning and the end of the j-th FOF branch by the factor $\varphi_j \text{mod}(2\pi)$.

Fig. 7 gives an overview of the dynamics in the SRL with an activated second FOF branch. Like in Fig. 6, the biasing of the second gate implies operation of the device on a related second channel

LM. The phase tuning φ_2, however, is a crucial factor determining which second channel LM will play a dominant role. It determines the relations between the phases of the fields propagating in the same direction along the ring and the second filtering branch at the interface J_s shown in Fig. 4. For constructive relations, a steady state operation determined by a single second channel LM can be observed, see, e.g., optical spectra at $\varphi_2/2\pi = 0.5$ in Fig. 7(c). Changing φ_2 induces some dislocation of these phase relations. It is compensated by some small shift of the lasing frequency (the related small shift of lasing wavelengths can be seen within the white area around $\varphi_2/2\pi = 0.5$ in Fig. 7(b)). Accordingly, a change takes place in the carrier densities and the optical field profiles in the ring and FOF branch. At some stage, further corrections of the same state are not possible anymore (the case of the state annihilation in the saddle-node bifurcation, for example), or the state loses its stability. In both cases, these bifurcations lead to some new dynamic states determined by another second channel LM or still by the same second channel LM which is now unstable.
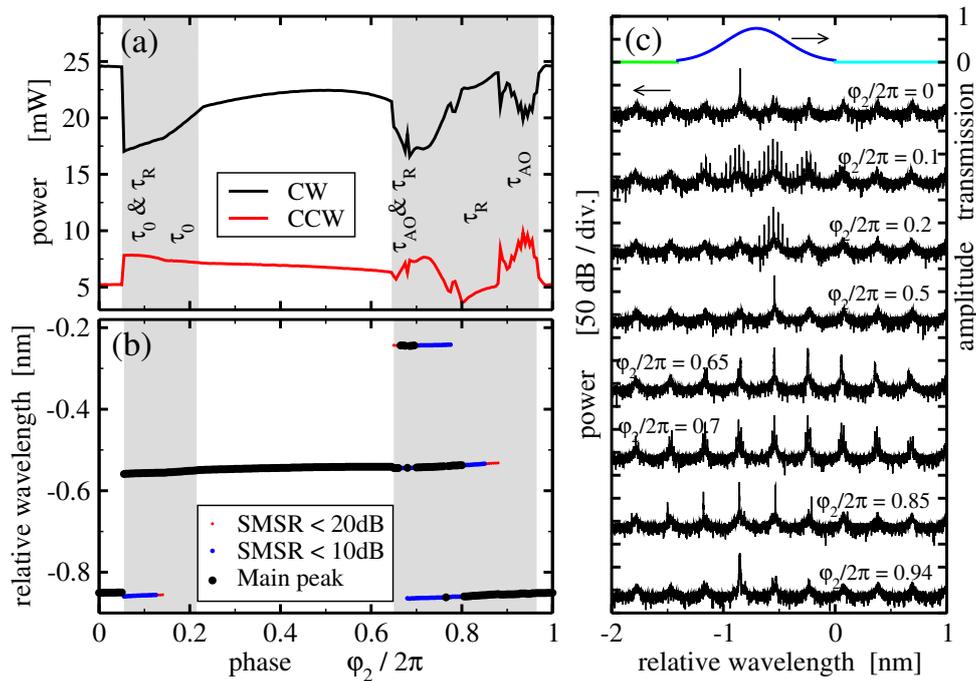

Figure 7: Simulated performance of the SRL with $I_R = 150\,\text{mA}$ and $I_2 = 80\,\text{mA}$ for different phase tuning factors φ_2. (a) and (b): mean intensities of both directional fields and main lasing wavelengths of the CW field as functions of φ_2, respectively. All notations are the same as in Fig. 5(a) and (b). Gray shading shows the regions where nonstationary, (mainly periodic or quasi-periodic oscillatory) regimes are observed. Characteristic periods of these states are indicated in panel (a). (c): selected optical spectra of the CW field for different phases φ_2. Typical transmission spectra for different FOF branches are plotted on the top of this panel.

Gray-shaded areas in Figs. 7(a) and (b) indicate regions of φ_2 where periodic, quasiperiodic or irregular oscillations of the field intensities could be observed. The main periods of these oscillations are indicated in the panel (a) of this figure, whereas optical spectra of typical representatives of these regimes are shown in Fig. 7(c). Oscillations with the ring roundtrip time τ_R are represented by two or even more large peaks of LMs ($\varphi_2/2\pi \approx 0.65$, 0.7, 0.85, and 0.1). The much slower oscillations with period $\tau_0 \approx 196\,\text{ps}$ at $\varphi_2/2\pi \approx 0.1$ and 0.2 are identifiable by multiple and still distinguishable equally separated spectral peaks close to one or several LMs. The AO period τ_{AO} at $\varphi_2/2\pi \approx 0.65$ and 0.94 is, approximately, 5.3 and $5.9\,\text{ns}$. Since the related spectral separations in these cases are $\Delta_{AO} \approx 1.57$ and $1.41\,\text{nm}$, they can be hardly distinguished in the corresponding spectra of Fig. 7(c).

Large deviations of τ_{AO} from the value observed in Fig. 6 (i.e. 2.75 ns) are due to different field distributions and, consequently, to different factors Δ_β.

Mode analysis [27, 21] of the considered device can give more insight into the origin of different oscillatory regimes. We expect that most of these oscillations are due to the beating of different *compound cavity* modes. The existence of the mode pair responsible for AOs in more simple ring laser configuration was explained in Ref. [21]. The reason for τ_0-periodic oscillations in our device could be the beating between the ring cavity modes and the supplementary modes introduced by the FOF. A complete mode analysis, however, is out of the scope of the present paper and will be reported elsewhere.

SRL with multiple activated branches of the FOF. Previously in this Section, we have demonstrated the selection of the lasing wavelength by the single activated FOF branch. In Fig. 8 we present a multicolor operation of the SRL with two or all four activated FOF branches. In all these cases, the SRL bias current is $I_R = 85$ mA.
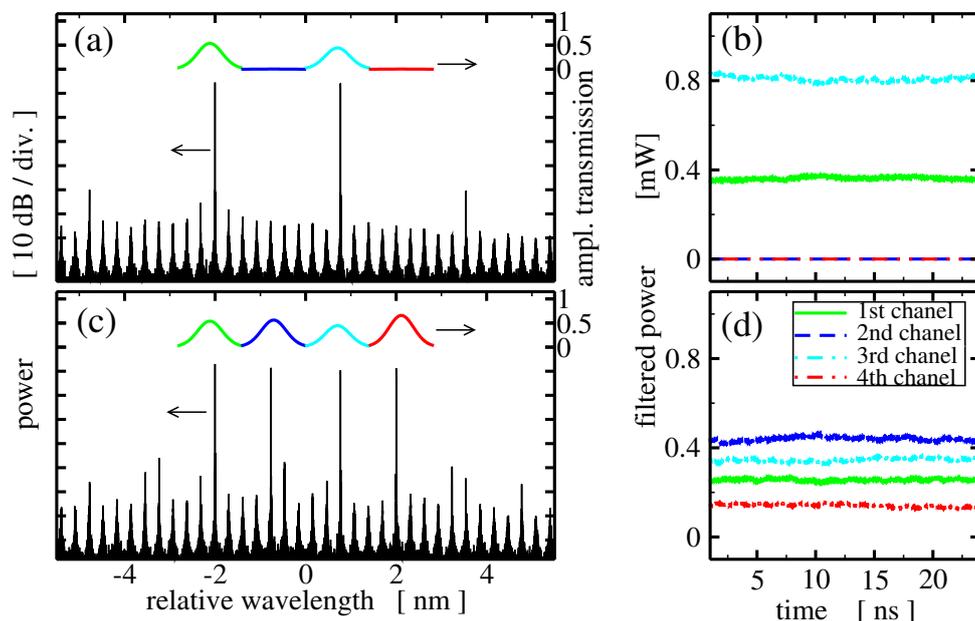

Figure 8: Simulated stable multicolor lasing of the SRL with $I_R = 85$ mA and the gate currents $(I_1, I_2, I_3, I_4) = (29, 0, 18, 0)$ mA (above) and $(29, 32, 18, 49)$ mA (below). (a) and (c): optical spectra of the CW emission (black) and transmission spectra for all four FOF branches (colored). (b) and (d): corresponding time-traces of the CW field after four digital filters centered at $\bar{\lambda}_1, \ldots, \bar{\lambda}_4$.

Fig. 8(b) confirms the stability of the simulated two-color regime. Two nonvanishing nearly horizontal curves in this diagram are almost constant time-traces of the CW emission radiated within the first and the third FOF frequency bands. Since the calculated emission naturally combines all LMs, for the extraction of the different frequency components of the field we have applied four different digital (Lorentzian) filters centered at the corresponding FOF peak wavelength $\bar{\lambda}$.

In the next step, we have additionally adjusted the second and the fourth FOF gate currents to $I_2 = 32$ mA and $I_4 = 49$ mA, respectively. All four FOF branches are opened in this case, see transmission spectra on the top of Fig. 8(c), and all these branches support their own LM, see four peaks in the optical spectra in the same figure. The stability of this state (nearly constant evolution of these four modes) is confirmed again by the panel (d) of the same figure.

It is noteworthy that the LM intensity depends on several factors. These are the field transmission through the corresponding FOF channel (bias of the corresponding gate); the mode gain in the SRL (Lorentzian gain peak position for $I_R = 85\,$mA used in our simulations was at $\bar{\lambda} = -1.6\,$nm); the amount of energy the LM gets from and transfers to the neighboring channel modes due to the FWM process; and the constructive or destructive relation between the phases of the complex fields in the ring and the FOF branch at the reinjection position.

State switching. Our next numerical experiment demonstrates switching between two different states, each supported by one of the FOF gates. Following Ref. [15], we have applied a constant injected current $I_3 = 15\,$mA at the third gate. We modulate I_2 between $10\,$mA and $25\,$mA using a $100\,$MHz NRZ step-wise modulation (see dash-doted curves in Fig. 9(a)) and keep the remaining gates unpumped. The main simulation results are summarized in Fig. 9.
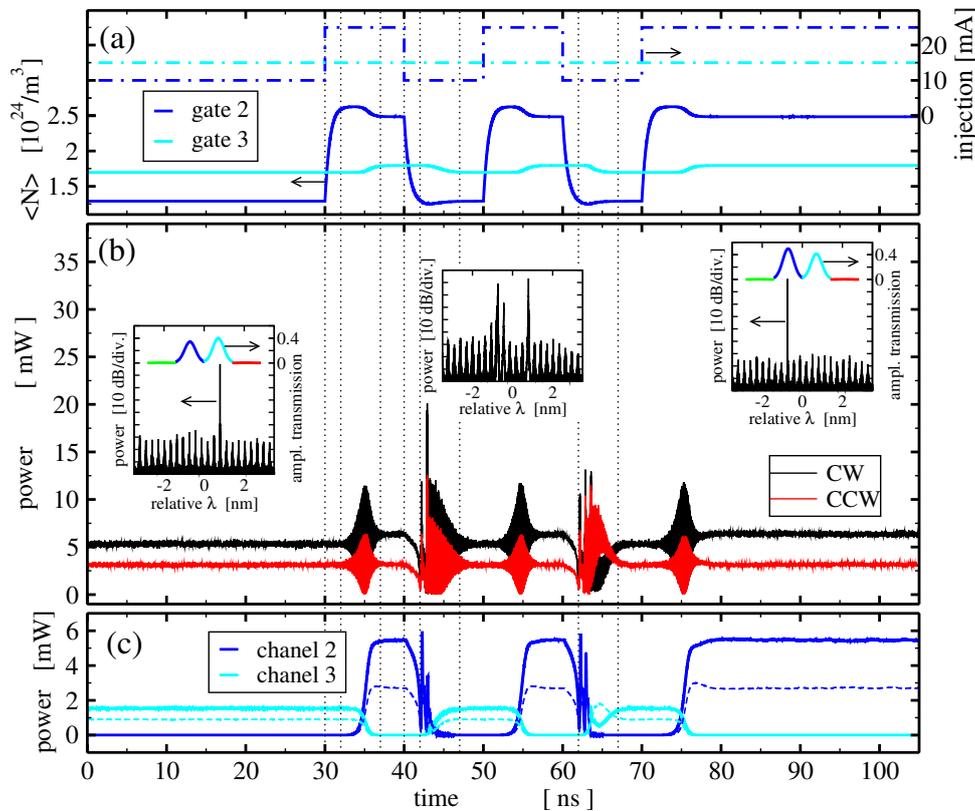

Figure 9: Simulated switching between different states of the SRL with $I_R = 95\,$mA by modulation of the second gate current. (a): Injected currents [dashed-dotted lines] and mean carrier densities [thick solid] in the 2nd and 3rd gates. (b): Emitted field intensity in CW [black] and CCW [red] directions. The inserts show the optical spectra of the CW emission and the corresponding field amplitude transmission through the different FOF branches before, during, and after the state switching. (c): CW (thick solid) and CCW (thin dashed) fields after the digital filters centered at $\bar{\lambda}_2$ (blue) and $\bar{\lambda}_3$ (cyan). Vertical thin dotted lines denote the time moments where some processes begin or end.

At the beginning of our simulations, the second gate was pumped with the constant $I_2 = 10\,$mA. Compared to the second gate, the pumping and the mean carrier density in the third gate are higher, see the left part of the panel (a). One of the third channel LMs in this case fully determines the steady-state lasing of the SRL. This state is represented by the optical spectra in the left insert of the panel (b) and the initial part of the differently filtered emission in panel (c) of Fig. 9.

An opposite situation takes place at the last part of the simulations. Here, $I_2 = 25$ mA, such that the second gate has the highest mean carrier density and one of the second channel LMs determines the lasing, see the right insert of panel (b) and the right-most part of panel (c).

In between, we apply a step-wise modulation of the second gate current. Each change of the bias current implies a large change of the carrier density in the second gate [panel (a)]. This change, in turn, significantly modifies the thresholds of the second channel LMs and causes the exchange of the operating states that can be seen in the middle part of Fig. 9(c).

In the considered example, there is around $6-7$ ns delay between the change of the injected current and the full change of the operating state, and there are at least two reasons for this delay. The first reason is the carrier recombination time within the gate to which current modulation is applied. After the change of pumping some time is needed before the carrier density adapts to this change, and the gain of the new mode overcomes the gain of the previously dominant one, see, e.g., time intervals $[30, 32]$ ns or $[40, 42]$ ns indicated by vertical thin dotted lines in Fig. 9. The second reason is an even longer time needed for the exchange of the field intensity between different LMs. Such a process can be rather simple and involve only the initial and the final mode, see, e.g., time interval $[32, 37]$ ns in Fig. 9, or, on the contrary, one can have a more complicated process involving additional modes. This more complicated case was observed within the time intervals $[42, 47]$ ns and $[62, 67]$ ns in Fig. 9. Here, besides the öldßecond channel LM and the "new"third channel LM, one has a significant contribution of the adjacent second channel LM, see the middle insert of Fig. 9(b).

The example above has shown an obviously distinguishable $\sim$100 Mbit/s NRZ current modulation induced switching between different channel modes. We believe that by an optimization of operating conditions we can double this rate. For a further increase of this rate, we should find out the mechanisms accelerating the power exchange between different operating modes.

5   Conclusions

In this paper, we have investigated an SRL that uses FOF as wavelength selection and tuning mechanism. By comparing experimental and theoretical results, we have demonstrated that the TW modeling approach is well suited for simulation of complex SRL configurations including several filtered optical feedback branches. In our simulations, we were able to recover and explain different static and dynamic effects of the considered device. These are asymmetric bidirectional lasing; multimode operation in the absence of feedback; mode selection by different FOF branches; multicolor lasing where lasing frequencies correspond to selected FOF branches; switching between operating states when tuning the SRL bias current or modulating current at the gate. We have also discussed different model parameters which are crucial when preparing the laser for the desired operation, e.g. we have shown how changes in the feedback phase need to be controlled. We believe that our work provides a perfect basis for future studies, and, in particular, that it provides some pointers for more detailed investigations on the different behavior of SRLs.

Acknowledgments

and J. Bolk from TUE for device fabrication in the framework of JePPIX.

References

[1] M. T. Hill, H. de Waardt, G. D. Khoe, and H. J. S. Dorren, "All-optical flip-flop based on coupled laser diodes," IEEE J. Quantum Electron. **37**, 405-413 (2001).

[2] M. T. Hill, H. J. S. Dorren, T. de Vries, X. J. M. Leijtens, J. H. den Besten, B. Smalbrugge, Y. S. Oei, H. Binsma, G. D. Khoe and M. K. Smit, "A fast low-power optical memory based on coupled micro-ring lasers," Nature, **432**, 206-209 (2004).

[3] S. Zhang, Y. Liu, D. Lenstra, M. T. Hill, H. Ju, G. D. Khoe and H. J. S. Dorre, "Ring-laser optical flip-flop memory with single active element," IEEE J. Sel. Top. Quant. **10**, 1093-1100 (2004).

[4] T. Butler, C. Durkan, D. Goulding, S. Slepneva, B. Kelleher, S. P. Hegarty, and G. Huyet, "Optical ultrafast random number generation using a turbulent semiconductor ring cavity laser," Opt. Lett. **41**, 388-391 (2016).

[5] S. Sunada, T. Harayama, K. Arai, K. Yoshimura, K. Tsuzuki, A. Uchida, and P. Davis, "Random optical pulse generation with bistable semiconductor ring lasers," Opt. Express. **19**, 7439-7450 (2011).

[6] W. Coomans, L. Gelens, S. Beri, J. Danckaert, and G. Van der Sande, "Solitary and coupled semiconductor ring lasers as optical spiking neurons" Phys. Rev. E. **84**, 036209 (2011).

[7] K. Grobe, M. H. Eiselt, S. Pachnicke and J. P. Elbers, "Access networks based on tunable lasers," J. Lightw. Technol. **32**, 2815-2823 (2014).

[8] L. A. Coldren, "Monolithic tunable diode lasers," IEEE J. Sel. Topics Quant. Elect. **6**, 988-999 (2000).

[9] L. A. Coldren, G. A. Fish, Y. Akulova, J. S. Barton, L. Johansson, and C. W. Coldren, "Tunable semiconductor lasers: A tutorial," J. Lightw. Technol. **22**, 193-202 (2004).

[10] J. Zhao, D. Lenstra, R. Santos, M. J. Wale, M. K. Smit and X. J. M. Leijtens, "Stability of a monolithic integrated filtered feedback laser," Optics. Express. **20**, B270-B278 (2012).

[11] B. Docter, J. Pozo, S. Beri, I. V. Ermakov, J. Danckaert, M. K. Smit, and F. Karouta, "Discretely tunable laser based on filtered feedback for telecommunication applications," IEEE J. Sel. Topics Quant. Elect. **16**, 1405-1412 (2010).

[12] S. Fürst, S. Yu, and M. Sorel, "Fast and digitally wavelength-tunable semiconductor ring laser using a monolithically integrated distributed Bragg reflector," IEEE Photon. Technol. Lett. **20**, 1926-1928 (2008).

[13] I. V. Ermakov, S. Beri, M. Ashour, J. Danckaert, B. Docter, J. Bolk, X. J. M. Leijtens, and G. Verschaffelt, "Semiconductor ring laser with on-chip filtered optical feedback for discrete wavelength tuning," IEEE J. Quantum Electron. **48**, 129-136 (2012).

[14] M. Khoder, G. Verschaffelt, R. M. Nguimdo, J. Bolk, X. J. M. Leijtens, and J. Danckaert, "Controlled multiwavelength emission using semiconductor ring lasers with on-chip filtered optical feedback," Optics. Lett. **38**, 2608-2610 (2013).

[15] M. Khoder, R. M. Nguimdo, J. Bolk, X. J. M. Leijtens, J. Danckaert, and G. Verschaffelt, "Wavelength switching speed in semiconductor ring lasers with on-chip filtered optical feedback," IEEE Photon. Technol. Lett. **26**, 520-523 (2014).

[16] M. Sorel, J. P. R. Laybourn, A. Scirè, S. Balle, G. Giuliani, R. Miglierina, and S. Donati, "Alternate oscillations in semiconductor ring lasers," Optics. Lett. **27**, 1992-1994 (2002).

[17] M. Sorel, G. Giuliani, A. Scirè, R. Miglierina, J. P. R. Laybourn, and S. Donati, "Operating regimes of GaAs- AlGaAs semiconductor ring lasers: experiment and model," IEEE J. Quantum Electron. **39**, 1187-1195 (2003).

[18] R. Lang, and K. Kobayashi, "External optical feedback effects on semiconductor injection laser properties," IEEE J. Quantum Electron. **16**, 347-355 (1980).

[19] M. Khoder, G. Van der Sande, J. Danckaert, and G. Verschaffelt, "Effect of external optical feedback on tunable micro-ring lasers using on-chip filtered feedback," IEEE Photon. Technol. Lett. **28**, 959-962 (2016).

[20] J. Javaloyes, and S. Balle, "Emission directionality of semiconductor ring lasers: a traveling-wave description," IEEE J. Quantum Electron. **45**, 431-438 (2009).

[21] M. Radziunas, "Longitudinal modes of multisection edge-emitting and ring semiconductor lasers," Optical and Quantum Electronics. **47**, 1319-1325 (2015).

[22] J. Javaloyes and S. Balle, "All-Optical Directional Switching of Bistable Semiconductor Ring Lasers," IEEE J. Quantum Electron. **47**, 1078-1085 (2011).

[23] A. Perez-Serrano, J. Javaloyes, and S. Balle, "Multichannel Wavelength Conversion Using Four-Wave Mixing in Semiconductor Ring Lasers," IEEE Photon. Technol. Lett. **25**, 476-479 (2013).

[24] X. J. M. Leijtens, "JePPIX: the platform for Indium Phosphide–based photonics," IET Optoelectron. **5**, 202-206 (2011).

[25] U. Bandelow, M. Radziunas, J. Sieber, and M. Wolfrum, "Impact of gain dispersion on the spatio-temporal dynamics of multisection lasers," IEEE J. Quantum Electron. **37**, 183-188 (2001).

[26] M. Radziunas, "Traveling Wave Modeling of Nonlinear Dynamics in Multisection Laser Diodes," in Handbook of Optoelectronic Device Modeling and Simulation: Lasers, Modulators, Photodetectors, Solar Cells, and Numerical Methods - Volume Two, J. Piprek, ed. (Taylor and Francis, 2017), pp. 153-182 [forthcomming]

[27] M. Radziunas, and H.-J. Wünsche, "Multisection Lasers: Longitudinal Modes and their Dynamics," in Optoelectronic Devices - Advanced Simulation and Analysis, J. Piprek, ed. (Springer, 2005), pp. 121-150.

[28] H.-J. Wünsche, M. Radziunas, S. Bauer, O. Brox, and B. Sartorius, "Simulation of phase-controlled mode-beating lasers," IEEE J. Sel. Topics Quant. Elect. **9**, 857-864 (2003).

[29] U. Bandelow, H. Wenzel, and H.-J. Wünsche, "Influence of inhomogeneous injection on sidemode suppression in strongly coupled DFB semiconductor lasers," Electronics. Letters. **28**, 1324-1325 (1992).

[30] M. Spreemann, M. Lichtner, M. Radziunas, U. Bandelow, and H. Wenzel, "Measurement and simulation of distributed-feedback tapered master-oscillators power-amplifiers," IEEE J. Quantum Electron. **45**, 609-616 (2009).

[31] V. Z. Tronciu, M. Lichtner, M. Radziunas, U. Bandelow, and H. Wenzel, "Improving the stability of distributed-feedback tapered master-oscillator power-amplifiers," IEEE J. Quantum Electron. **41**, 531-537 (2009).

[32] T. Krauss and P. J. R. Layboum, "Very low threshold current operation of semiconductor ring lasers," in Proceedings of IEEE Conference on International Semiconductor Laser (IEEE, 1992), pp. 383-388.